Research Article

Kanchan Yadav, Megha Das, Nitesh Kumar Mishra, Anuj Chhabra, Archana Mishra, Sunita Srivastava, Poonam Sharma*, Sanjeev Kumar Yadav, and Avanish Singh Parmar*

Tunning self-assembled phases of bovine serum albumin *via* hydrothermal process to synthesize novel functional hydrogel for skin protection against UVB

https://doi.org/10.1515/ntrev-2022-0102
received December 30, 2021; accepted March 28, 2022

Abstract: Ultraviolet rays – B (UVB) can be efficiently absorbed by the cellular molecules of skin inducing damage within skin cells and a major cause of melanoma cancer. In recent years, several studies have reported the adverse effects of traditionally used organic and inorganic material-based sunscreens and UVB blockers. In this study, bovine serum albumin (BSA) has been used as a precursor to synthesize temperature- and pressure-dependent phase transition from sol (globular aggregates) – gel (hydrogels) – sol (carbon quantum dots) using a single-step hydrothermal method with an objective to develop an efficient and effective UVB blocker. The synthesized hydrogels exhibit UV – attenuation, self-fluorescence, and high biocompatibility properties that make them a suitable candidate for UV-blocker or sunscreen material. The biological efficacy of the hydrogels was studied through cyto-toxicity studies. Also, UVB blocking efficiency of developed hydrogel in primary mice skin cell culture as well as *in vivo* in mice model was studied. *In vivo* study on mice further demonstrated prominent thickening of stratum corneum and epidermis with perivascular edema in the dermis after 5 days of UVB exposure. Hence, this suggesting that hydrogel could be a potential candidate for protecting the skin from UVB exposure and reducing the threat of skin cancer.

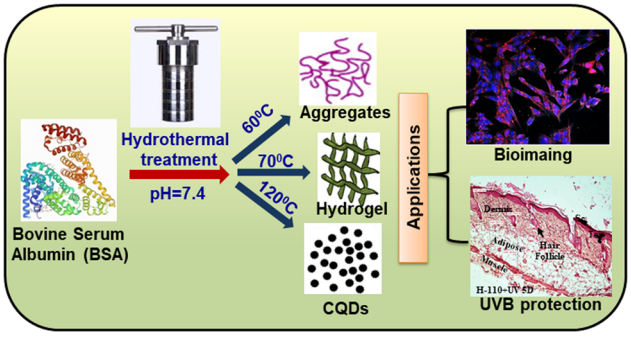

Graphical abstract

Keywords: hydrogel, self-assembly, skin protection, UVB

*** Corresponding author: Poonam Sharma,** Department of Dravyagun, Faculty of Ayurveda, Institute of Medical Sciences, Banaras Hindu University, Varanasi, India,
e-mail: poonamsharma@bhu.ac.in
*** Corresponding author: Avanish Singh Parmar,** Department of Physics, Indian Institute of Technology (BHU), Varanasi, India; Centre for Biomaterials and Tissue Engineering, Indian Institute of Technology (BHU), Varanasi, India,
e-mail: asparmar.phy@itbhu.ac.in
Kanchan Yadav: Department of Physics, Indian Institute of Technology (BHU), Varanasi, India
Megha Das, Nitesh Kumar Mishra, Sanjeev Kumar Yadav: Department of Zoology, Institute of Science, BHU, Varanasi, India
Anuj Chhabra: Centre for Research in Nanotechnology and Science, Indian Institute of Technology, Bombay, India
Archana Mishra: Nuclear Agriculture and Biotechnology Division, Bhabha Atomic Research Centre, Mumbai, India
Sunita Srivastava: Department of Physics, Indian Institute of Technology, Bombay, India

1 Introduction

Skin, the largest organ in the body, has a surface area of about 1.8 m^2 and occupies 16% of the total body mass of an adult [1]. The primary and most important function of the skin in mammals is to provide a protective barrier against various infections caused by fungi, bacteria, UV radiation, and other environmental factors [2]. One of the major reasons for skin cancer is exposure to UV radiation (UV) which is classified as UVA (320–420 nm), UVB (290–320 nm), and UVC (200–290 nm). Almost all three, UVC and a part of UVB wavelength get absorbed by the ozone layer and limit their reach upto the earth's surface

[3,4]. UVA has a minor effect on the skin; however, UVB is the primary threat to human health and is responsible for skin cancer, photoaging, immune suppression, and sunburns [5,6].

Cancer is the most challenging disease to treat and the second most cause of mortality in the world. In recent years, there is a tremendous increase in skin cancer worldwide [7,8]. The major types of skin cancers are basal cell carcinoma, squamous cell carcinoma, Markel cell cancer, and melanoma in which melanoma is most dangerous because of its ability to spread faster to other organs if it is not diagnosed at an early stage and even becomes deadly [9,10]. Therefore, treating melanoma skin cancer is a big challenge, and emerging functional materials give a possible route to treat melanoma by enhancing drug uptake in cancer cells, minimizing toxicity, increasing the circulation time in tumor tissue, *etc*.

Avoiding excessive solar exposure and using sunscreens composed of nanoparticles such as zinc oxide NPs, are recommended to prevent exposure to UV radiation [11–13]. Currently, the most commonly used sunscreens are based on the nano-sized TiO_2 and ZnO nanoparticles [14,15]. Skin exposure to the nano-sized particles containing sunscreens leads to the incorporation of inorganic material in the stratum corneum which can alter the attenuation properties due to particle-particle, particle-skin, and skin-particle-light physiochemical interactions [16,17]. Photocatalytic effects, nanoparticle stabilization after chronic exposure, and free radical production are some other major concerns to using these materials as sun blockers. The current scenario demands a new alternative material for skincare treatments, which can be more efficient, biocompatible, minimizing the side effects, and reducing the treatment cost significantly for the patients [18–21]. In this regard, functional biomaterials could be a good alternative to the nano-sized inorganic nanoparticle to prevent sunburns and skin cancer.

Proteins are biomolecules in nature; thus, they are safe and biocompatible. In recent studies, proteins have been extensively utilized by Materials scientists to design novel materials with unique functionality that further improves their practical applicability [22–25]. The complex structure of proteins is maintained due to the various interactions such as electrostatic, van der Waals, hydrophobic, and cation-pi. This gives tremendous opportunity to tune them into self-assembled hierarchal structures. Another fascinating aspect of self-assembled protein materials is the formation of hydrogel, which have multifunctional properties [26–29]. Protein-based hydrogels are a promising material for various biomedical applications because of their hydrophilic networks, controllable self-assembly, and biocompatibility. Bovine serum albumin (BSA) is a cost-effective, easily, and widely available protein. Its primary structure contains a single polypeptide chain of 583 amino acids with a molar mass of 66.4 kDa. BSA is a water-soluble protein with 76% sequence homology and identical pH-dependent conformation with human serum albumin [30,31]. Studies show that BSA has been conjugated with many organic and inorganic compounds for the synthesis of bio-nanoconjugates, monolayers, and nanoparticles, and holds promising applications in the biomedical field [32–36].

Thus, BSA has been used as a precursor to synthesize different self-assembled morphologies using a single-step hydrothermal thermal method with an objective to develop an efficient and effective UV-B blocker. By varying the hydrothermal temperature from 25 to 120°C, different phases of BSA protein have been synthesized. First, sol-to-gel transition occurs at 70°C, where BSA protein transforms into a self-assembled hydrogel phase, further heating of BSA protein at 120°C leads to the second-phase transition from gel to carbon quantum dots. Developed phases were thoroughly characterized using various physical and optical techniques such as SEM, TEM, FTIR, and SAXS, for studying their efficient applicability in the biomedical field. Biological efficacy was studied through cytotoxicity studies, and UV-B blocking efficiency of developed hydrogel was studied in primary mice skin cell culture as well as *in vivo* in mice model.

2 Material and methods

2.1 Chemicals and materials

BSA (lyophilized powder, >96% (agarose gel electrophoresis), M_W = 66,430 Da), rutile nanosized TiO_2, sodium chloride, hydrochloric acid, disodium hydrogen phosphate, and sodium dihydrogen phosphate were purchased from Sigma-Aldrich and used without further purification. Deionized water (12M-cm) from the Millipore water purification system was used for all aqueous solution preparations.

2.2 Synthesis of temperature-dependent phases of BSA

All the temperature-dependent phases of BSA were synthesized using the single-pot hydrothermal method. The homogenous solutions of concentration 40 mg/mL of lyophilized BSA powder were prepared using Sorensen's phosphate buffer (pH-7.4) with a sodium salt concentration of 150 mM.

The prepared solutions were transferred to a 25 mL Teflon cylinder with a steel autoclave and heated for the hydrothermal reaction at temperature ranges from 25 to 120°C for 15 h. During heating at different temperatures, different phases of BSA were resulted. The resultant samples were named according to their heating temperature, for example, H-100 suggests that BSA solution has been heated at 100°C for 15 h using the hydrothermal method.

2.3 Characterization techniques

A different phase of BSA has been characterized using suitable physical techniques. UV-Vis measurements have been performed using JASCO V770 UV-Vis spectrophotometer and Eppendorf Biospectrometer for solid and liquid samples, respectively. Photoluminescence (PL) properties have been studied using Fluorolog (Horiba). Fourier transform infrared (FT-IR) spectroscopy was performed using the Thermo Scientific Nicolet iD7 spectrometer over the wavenumber 500–4,000 cm^{-1} region with a resolution of 4 cm^{-1}. Field emission scanning electron microscope (FESEM) images were taken using a FEI Nova NanoSEM 450 FESEM. A transmission electron microscopy (TEM) image was obtained using the TECNAI-T-20 (FEI instrument) at 200 kV accelerating voltage. LV100ND fluorescence microscope and Carl Zeiss 780 LSM laser scanning confocal microscopy system (Germany) were used for fluorescence microscopy. Rheological characterization of BSA hydrogels was performed using the Anton Paar Physica MCR301 rheometer. The BSA hydrogels were prepared in a hydrothermal autoclave and transferred to the rheological geometry of 8 mm parallel plates having a gap of 1 mm at room temperature for further studies. The measurement for storage and loss modulus as a function of strain and frequency was also performed for all hydrogels (H-70 to H-110) between the frequency range of 0.1 and 10 rad s^{-1} with a constant strain of 0.5% at 25°C. Xenocs SAS, model Xeuses 2.0, with a dual-source module X-ray source (Q range varies from 0.005 to 1.2 Angstrom^{-1}) was used for the small-angle X-ray scattering (SAXS) measurement.

2.4 *In vitro* studies

2.4.1 Cell culture

For primary skin cell culture, skin tissue was collected from the hairless skin of Swiss albino mice, and the isolation of primary epidermal cells, endothelial cells, dermal cells, and fibroblast cells was performed by following the protocol given by Pauline Henrot *et al.* [37]. For experimental purposes, epidermal cells were used.

2.4.2 Cell viability

The biocompatibilities of all samples, *i.e.*, H-25, H-60, H-70, H-80, H-90, H-100, H-110, H-120, and H-200, were determined by the MTT [3-(4,5-dimethylthiazol-2-yl)-2,5-diphenyl tetrazolium bromide] assay where the primary mice skin cells were plated at 10^4 cells/well in 96-well plates (Genetix) 24 h prior to the experiments. After completion of 24 h, the cells were treated with H-25, H-60, H-70, H-80, H-90, H-100, H-110, H-120, and H-200 with the same dose (20 mg/mL, *i.e.*, 1:1 sample: complete media). In control (with cells) and negative control or blank (without cells) groups, the complete media were added. After 24 h of treatment, the cells were processed for the MTT assay following the laboratory standard process [38], and the optical density was measured in triplicate at 595 nm in a microplate reader (Biorad).

2.4.3 Cellular uptake

For the cellular uptake study of each sample, primary mice skin cells were seeded at 6,000 cells/well upon the round coverslips placed inside the 24 well plates 24 h prior to treatments. After 24 h, the cells were treated with the samples (H-25, H-60, H-70, H-80, H-90, H-100, H-110, H-120, and H-200) at the concentration of 20 mg/mL for the next 24 h similarly to MTT assay. After completion of 24 h, treated cells were fixed, permeabilized, and stained with DAPI according to the laboratory standard procedure [39], and finally, images were captured by a Carl Zeiss 780 LSM laser scanning confocal microscope (Germany).

2.4.4 UVB treatment study

An UVB lamp (G25T8E, Sankyo Denki) with peak emission at 306 nm was used for the generation of UVB radiation. For the UVB treatment study, the whole experiment was divided into two primary groups, *i.e.*, UVB treated and UVB + H-110 treated. Each group was further subdivided into three subgroups according to UVB exposures, *i.e.*, 5, 10, and 15 min according to ref. [17]. For each subgroup, primary mice skin cells were seeded at 6,000 cells/well on coverslip (3 wells) and 12,000 cells/well in other 3 wells of 6 well plates [thus 3 separate 6-well plates for 5′, 10′, and 15′ UVB treatment] for 24 h for acclimatization. After the completion of 24 h, every six-well plates was

placed under UVB light of the self-made UVB chamber (Figure S1) for respective 5′, 10′, and 15′ UVB treatment. On the same day, the cells of the UVB + H-110 group were first layered and incubated with H-110 for 1 h inside the CO_2 incubator. After 1 h, the cells were treated with UVB as described earlier. After all treatments, the cells seeded on the coverslips were fixed permeabilized and stained with DAPI, and the images were captured by a Carl Zeiss 780 LSM laser scanning confocal microscope (Germany) for cytological study. Other treated cells were processed for survival analysis through MTT assay.

2.5 *In vivo* mice model study

Two weeks prior to experimentations, all-female Swiss albino mice (N = 30) were maintained at 12 h light: 12 h dark cycle with 25 ± 2°C temperature at the Department of Zoology, Banaras Hindu University, Varanasi, Uttar Pradesh, India. All maintenance procedures along with experimentations were performed following the revised Animals Act Government of India, 2007, approved rules [Committee for the Purpose of Control and Supervision of Experiments on Animals (CPCSEA), Registration No. 1802/GO/Re/S/15/CPCSEA].

After acclimatization, animals were divided into six following groups with five animals in each group:

1. Control (n = 5) – without any treatment,
2. H-110 treated group (n = 5) – where a single layer of H-110 at the backside was applied to each animal,
3. 3 days UVB-treated group (UV 3D, n = 5), treated with UVB for 20 min for 3 days,
4. 5 days UVB-treated group (UV 5D, n = 5), treated with UVB for 20 min for 5 days,
5. 3 days H-110 + UVB-treated group (H-110 + UV 3D, n = 5), where a single layer of H-110 at the backside was first applied and then the UVB treatment was given for 20 min for 3 days,
6. 5 days H-110 + UVB-treated group (H-110 + UV 5D, n = 5), where a single layer of H-110 at the backside was first applied and then UVB treatment was given for 20 min for 5 days.

During treatment, mild ether anesthesia was continually given to the animals. After completion of the experimental periods, part of the treated skin was collected from each animal for further histoarchitectural analysis. No animals were sacrificed during this experimentation; as after skin collection, animals were given proper medical care to heal the wounds.

2.5.1 Morphometric analysis

For histological analysis, skin were immediately removed from each group of animals and fixed in 10% formalin, followed by dehydration, clearing with xylene, and finally processed in wax and sectioned (7 microns) for hematoxylin and eosin staining (HE staining) [39]. Histoarchitectures were observed under a research microscope (Nikon E 200, Japan) in randomly selected sections.

3 Results and discussion

3.1 Sol–gel–sol transformations of BSA hydrogel

BSA gels were prepared at different hydrothermal temperatures varying from 25 to 120°C with the 40 mg/mL protein concentration without using any cross-linker or chemical agent. At 25°C, the BSA solution does not go for the gelation process even after 15 h of heating, and the resultant has the same sol phase as the BSA initial solution. Further heating at 60°C, the turbidity of the solution is increased; however, no gelation occurs. One of the plausible reasons is that below the melting temperature (63°C), protein starts to unfold and thermal energy and electrostatic forces between the amino acid start to encounter each other during the hydrothermal process [40]. The melting temperature of the BSA is above 63°C, so the BSA solution was heated at 70°C hydrothermally for 15 h. Heating protein solution at a temperature of 70°C changed the turbid sol phase into a very fine gel, and this gel phase remains till the temperature of 100°C. Further heating of the protein solution above 110°C leads to the formation of new phases, and the phase separation between sol and gel was observed. The major portion of the protein solution changes into gel but the color of the gel becomes brownish and the remaining liquid was white. When the protein solution was heated to 120°C, the whole protein solution was converted into a sol phase and shows the physical and optical properties of carbon quantum dots. All the phases of the BSA are shown in Figure 1.

The sol–gel–sol phase transition as a function of temperature was tested using the tube inversion method. Thermally elevated phases of BSA show sol-to-gel and gel-to-sol transformation at 70 and 120°C, respectively. The melting temperature of BSA is 63°C, and studies show that BSA has different oligomeric states above and below its melting temperature [41]. The heating of proteins above melting temperature results in weakening

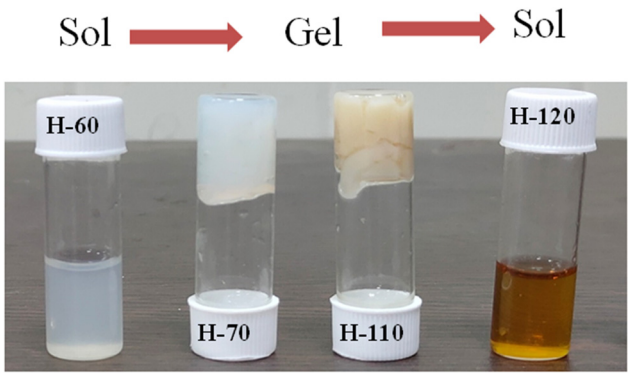

Figure 1: Different phases of developed BSA hydrogel at different temperatures.

the hydrogen bonds and strengthening the hydrophobic interaction which alters the diffusion, accessibility, and exposure of polypeptide chains segment and dilutes the ligand binding properties [42]. Interactions between electrostatic and hydrophobic interaction result in connecting the protein molecules and led to form a gel-like structure. The aggregation of BSA can be elevated with temperature, pH, ionic strength, and other external stimuli. These factors play a significant role in the transition temperature of the various phases. As we heat the protein solution at a higher temperature, the strength of the gel decreases, which was further supported by rheological studies and a tube inversion test. At high temperatures, interactions present between the gels start to break, and gel-to-sol phase transition happens. Physical and optical characterizations of the sol phase confirm the nanostructure of the carbon quantum dots that are homogeneously dispersed in the medium [42,38]. Thus, different phases of BSA hydrogels have been synthesized using a single hydrothermal technique just by varying temperatures without the addition of a cross-linker molecule.

3.2 Optical characterization of various phases of BSA hydrogels

It was observed that all the BSA hydrogels synthesized at various temperatures show different colors in appearance. As the heating temperature increases, there is a change in color. It becomes a transparent solution to translucent white in the gel phase and dense yellow in the CQDs phase. UV-Vis spectroscopy was used to analyze the optical changes shown in Figure 2(a). UV-Vis spectra of H-25 (hydrogel synthesized at 25°C) show the typical characteristic peak of BSA observed at 278 nm. As there is an increase in the temperature, protein starts to aggregate and forms a gel. H-70 (hydrogel synthesized at 70°C) and H-110 (hydrogel synthesized at 110°C) also show the BSA peak but absorb in a broader range from UV to visible, which make them a suitable candidate for skin protection from UVB (Figure S2(a)). H-110 shows a new peak at 340 nm, which reveals the possibility that there might be a generation of new fluorescent compounds during the gelation process. H-120 shows the characteristic peak of CQDs at 275 nm which is due to the $\pi-\pi^*$ electronic transition of C=C on the CQDs surface. The board absorbance shows the presence of a large number of functional moieties present on the surface. Figure 2(b) shows the auto-fluorescence property of various phases of BSA. It is well established that BSA has blue auto-fluorescence because of the aromatic amino acids such as tyrosine, tryptophan, and phenylalanine [43]. The emission spectra of H-25 and H-60 show intrinsic fluorescence such as BSA solution centered at 340–350 nm with the excitation wavelength of 280 nm. The excitation spectrum is also centered at 270–290 nm and does not show long-range excitation. Moreover, the gel phases of the BSA (H-70 to H-110) exhibit a strong fluorescence at 450 nm when excited with 365 nm. The PL spectrum of the gels (Figure S2(b)) shows a redshift in excitation and emission compared to the sol phase. The emission spectrum ranges from 400 to 550 nm for emission with the broad excitation wavelength ranging from 325 to 375 nm. This phenomenon can be explained by the fact that the heating of the protein reduces the steric hindrance of peptide chains and exposed the aromatic amino acids that can favor the energy transfer among the C=C and C=O bonds that existed in the protein as well as the proximity of amine groups. Another reason could be the formation of new fluorophores that have been promoted by the temperature-induced gelation process. The intensity of the fluorescence also increases with the hydrothermal temperature but does not show a strong redshift. Due to the presence of a larger number of amino acids and the non-availability of information regarding their interactions, it is difficult to probe the accurate reason for the red-shifted and high auto-fluorescence intensity in hydrogels. The CQDs phase of the BSA shows a blue shift in excitation and emission wavelength compared to the gel phase which can be tuned by concentration and excitation wavelength. Wavelength-dependent emission in CQDs can be due to the non-uniform size distribution in dispersive medium and various surface functional groups such as carboxyl, hydroxyl, and other oxygen species.

To get more insight into the involvement of various functional groups to form different phases of BSA at various temperatures, FTIR analysis has been performed.

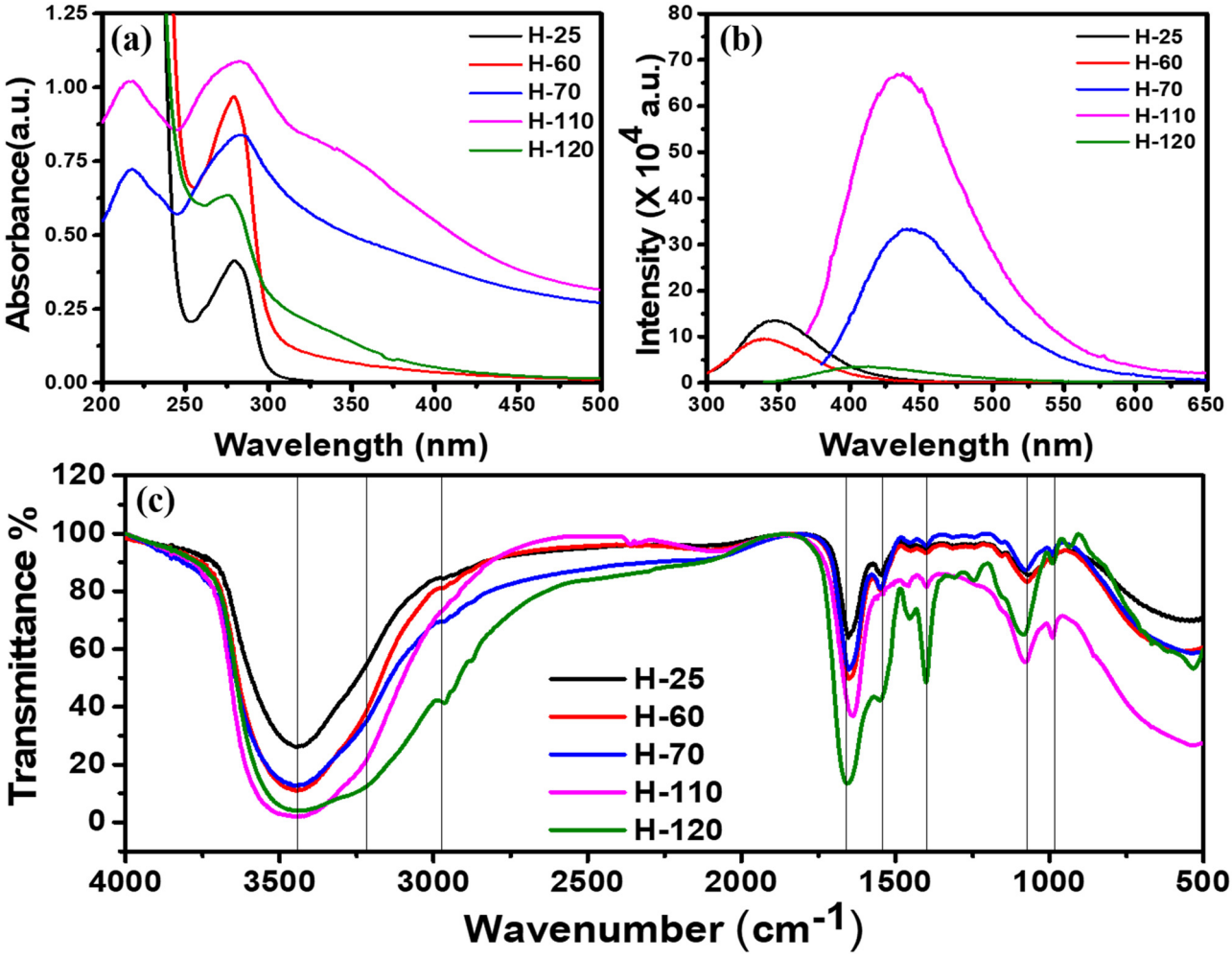

Figure 2: (a) UV-Vis spectrum of different phases of BSA protein; (b) PL spectrum of different phases of protein at their maximum excitation wavelength; (c) FTIR spectrum of different phases.

Full scan FITR spectra (4,000–500 cm^{-1}) of all phases of BSA are shown in Figure 2(c). Intensity variation and small spectral shifts have been observed during the gelation process, and some new peaks have been observed when the gel phase is converted to CQDs. The broad peak at 3,500 cm^{-1} corresponds to the amide II bond due to the N–H stretching present in all the phases. From the sol-to-gel transition, only the peak becomes broader, but during the gel to CQDs transition, new peak occurs at 3,252 cm^{-1} corresponding to the N–H bond of the amine ($-NH_2$) group. Amide band (1,400–1,700 cm^{-1}) exists during both phase transitions and supports the fact that the protein main chain remains intact after heating at high temperature [44]. Peaks due to amide I bond C═O stretch at 1,650 cm^{-1} become strong with gel formation but amide II bond (C–N stretch coupled with N–H bending) at 1,580 cm^{-1} disappears in gel; however, it becomes stronger in the CQD phase. The decrease of amide II at approximately 1,580 cm^{-1} and increase of Amide II at approximately 1,450 cm^{-1} are related, which shows the conformational changes at a tertiary structural level. CQDs are nano-dimensional structural with an exposed functional group on the surface. The very strong peak around 1,400 cm^{-1} in the CQD phase corresponds to the symmetric stretching vibration of COO–, which disappear in gel form due to the CO–NH bond formation and also the peak at 1,093 cm^{-1} due to C–O vibration becomes prominent in the CQD phase. The limitation of the FTIR instrument investigation of new chemical bond formation overrules and limits the accurate analysis of the sol-to-gel transition.

SAXS has been performed on the samples prepared namely H-25, H-60, H-70, H-90, H-110, and H-120. No gel formation was observed in the samples prepared at the temperatures 25 and 60°C, and they remained in the solution state. On the other hand, gel formation was observed in the samples, which was prepared above the transition temperature. Raw data for the samples are shown in

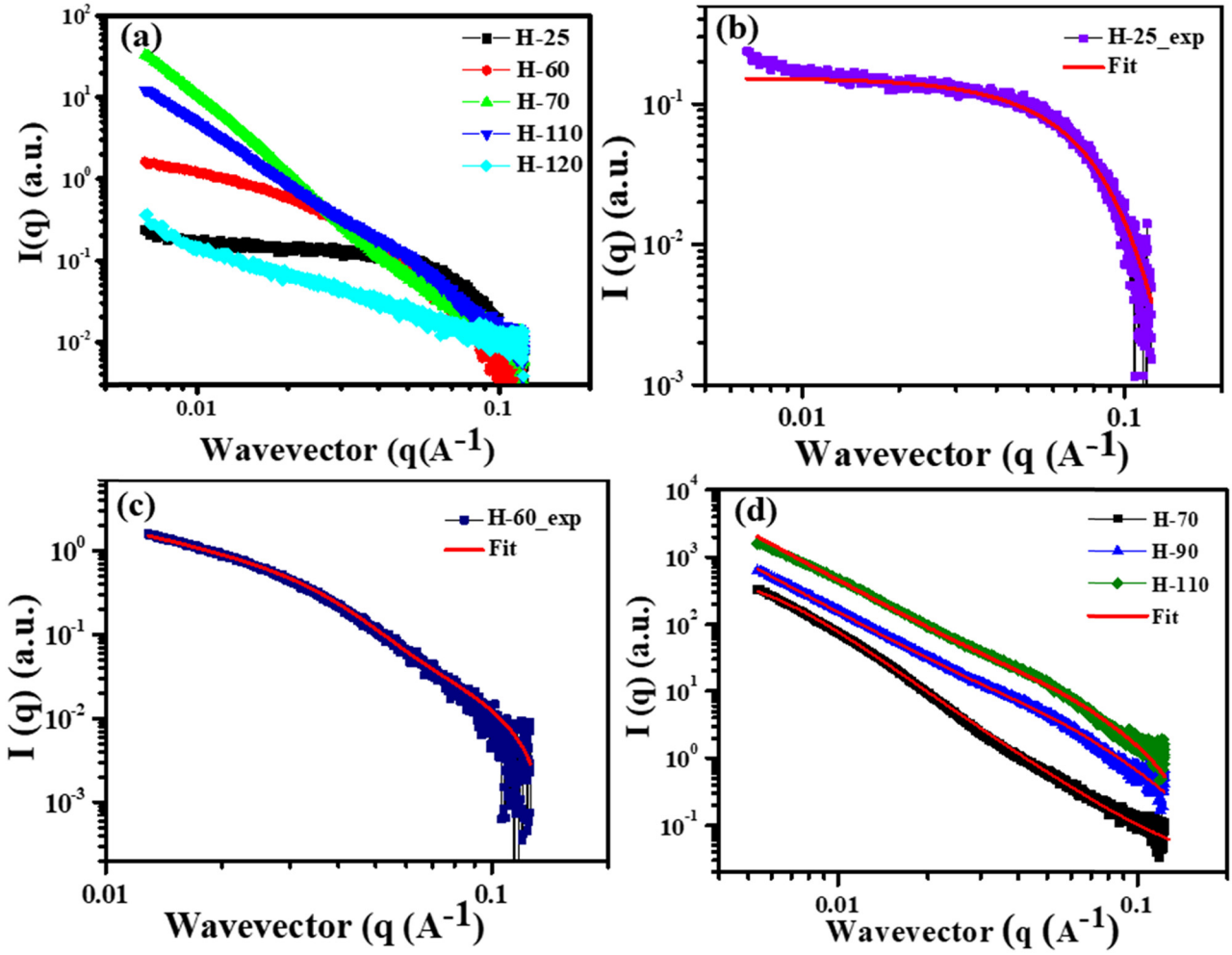

Figure 3: (a) Small-angle X-ray diffraction analysis of all phases of BSA protein; (b) shows that fitting of the SAXS of the H-25 samples using the spherical model; (c) H-60 is prepared near the transition temperature, SAXS for H-60 is fitted using the combination of Lorentz and Guinier equation; (d) shows the fitting of H-70, H-90 and H-110 using the Lorentz and porod fitting.

Figure 3(a). Sample H-25 shows a characteristic curve for a sphere. BSA in the solution state was found to form a globular structure, and the radius of the globule has been calculated by fitting the spherical model. The calculated radius of the BSA is found to be 3.198 nm. The fitted data are shown in Figure 3(b).

For the sample H-60, it is near the phase-transition temperature. It was observed that it was neither showing the characteristic curve for a sphere nor a gel. As the samples are prepared near the phase transition temperature, it can be assumed that SAXS data will be a combination of both the solution state sample and hydrogels. The mathematical equation used to fit the curve is given by equation (1) [45]:

$$I(q) = \frac{I(0)C}{1 + \left[\left(\left(D + \frac{1}{3}\right)(q^2 a_1^2)\right)\right]^{\frac{D}{2}}} + I(0)Gexp^{(-q^2 a_2^2)}, \quad (1)$$

where $I(0)$ is the scaling factor, C is the Lorentz scale, G is the Guinier scale, a_1 is the correlation length, a_2 is related to the radius of gyration of the globule structures of the BSA formed and can be given as $a_2^2 = R_g^2/3$, and D is the fractal dimension of the system.

The fitted curve for the H-60 is shown in Figure 3(c). Fitted parameters for the H-60 are listed in Table S1. The value of D indicates the solvent condition. D value greater than 2 indicates a bad solvent condition; D value less than 2 indicates that the BSA is in good solvent condition and equal to 2 indicates that BSA is in the theta solvent condition. For the H-60 sample, the value of D is 1.75 which is close to the value of 5/3 indicating that the BSA below the transition temperature is in good solvent condition. a_1 indicates the mesh size of the crosslinks formed. The fitted mess size comes out to be 22 nm. The R_g^2 value calculated is 5.9 nm. From this fitted data, it can

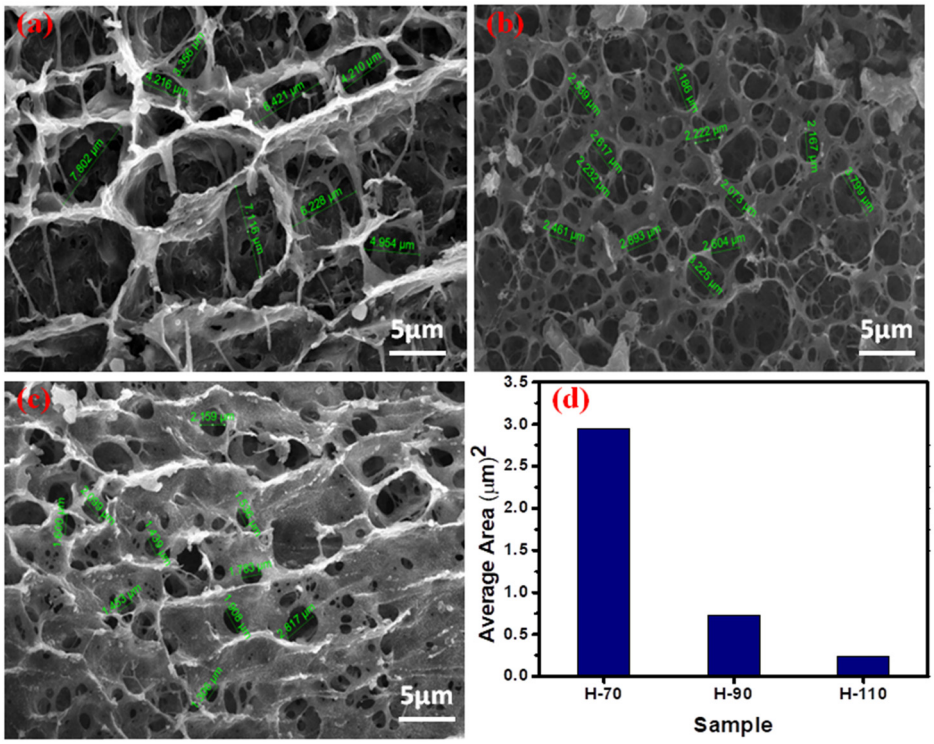

Figure 4: SEM images of hydrogel: (a) H-70; (b) H-90; (c) H-110; and (d) histogram of the area of voids.

be confirmed that near the transition temperature BSA molecules start to swell and start to form the network. The force between the molecules is not strong enough to form a strong network of BSA. Thus, there is a possibility of the existence of both globular structures along with a mesh. For gel samples, namely H-70, H-90, and H-110 fitted data are shown in Figure 3(d). To fit the experimental data, equation (2) has been used [46–48].

$$I(q) = \frac{A}{q^n} + \frac{C}{(1 + (q \star a_1)^m}, \tag{2}$$

where A is the porod constant, C is the Lorentz constant, n is the porod factor, m is the Lorentz factor, and a_1 is the mesh size.

The fitting parameters are shown in Table S2. n is the factor that corresponds to t homogeneity of the system. n value above 2 indicates that formed gels are homogeneous. As the temperature is increased, the value of n also increases indicating that with an increase in temperature, BSA molecules unfold and form a homogeneous structure. For H-70, as the temperature is closer to the transition temperature, n is a little less than 2 which indicates that the gel structure is not fully homogeneous and the interaction between the molecules to form the crosslinks is not strong enough. For samples H-90 and H-110, the n value is above 2, and it indicates that the samples are homogeneous, and the bonds are strong enough to form the crosslinks to form stable hydrogels.

Lorentz part of the curve has two parameters m and a_1. Lorentz factor m suggests the interaction of the molecules with the solvent. m above the value of 2 indicates that the molecules are in poor solvent condition, and the interaction between the molecules is dominating. As the temperature is increased, m value also increases indicating that the molecules are coming together to form the denser crosslinks. a_1. value is found to decrease with an increase in temperature which tells us that the distance between the crosslinks is decreasing. Therefore, this indicates that gels formed at higher temperatures are much denser. Also, for the H-70 sample, as the temperature is near the phase transition, mess size is larger when compared with samples prepared at a higher temperature. This indicates that gels formed are not very dense, and the bonding between the molecules is not strong enough to form denser gels. For H-120, SAXS scattering is very weak and is very close to the background; so, it is not possible to analyze the same.

To investigate the surface morphology and mechanical strength of the temperature elevated self-assembled hydrogels, SEM and rheology studies were employed. The SEM images of lyophilized powder of BSA hydrogels (H-70, H-90, H-110) are shown in Figure 4(a)–(c). All

hydrogel phases exhibit a three-dimensional highly porous honeycomb-like structure with irregularities in shape and size. During the lyophilization process, water gets evaporated and lefts the voids between the interconnected areas [49]. As there is an increase in the hydrothermal temperature, the pore size of the hydrogels gets smaller. Relative decreases in pore size of hydrogels are shown in Figure 4(d).

3.3 Rheological analysis

Rheological studies have been performed to investigate the viscoelastic behavior of the hydrogels. Strain sweep test and frequency sweep test were performed to get insight into change in storage and loss modulus of gels as a function of strain and frequency. To evaluate the limits of the viscoelastic region, strain sweep tests were carried out on all the hydrothermally synthesized gel phases of BSA. In the linear viscoelastic region, the storage modulus G' and viscous modulus G'' are independent of strain and frequency [50]. Under higher strain conditions, the stress response of the gels is no longer sinusoidal, and similarly, higher harmonic contributions lead to a nonlinear stress–strain relationship. In the case of the strain sweep test, G′ and G″ were plotted as a function of strain (%). As we increase the hydrothermal temperature from 70 to 90°C, both G′ and G″ increase linearly as shown in Figure 5(a). However, at 100°C, the G′ and G″ start to decrease, which suggests that due to the hydrothermal process, the lower-order structure starts to form that alters the viscoelastic property of hydrogel. Also, for the H-110 phase, we are getting similar viscoelastic trends as H-70. Additionally, in the case of the frequency sweep test, both G′ and G″ moduli also

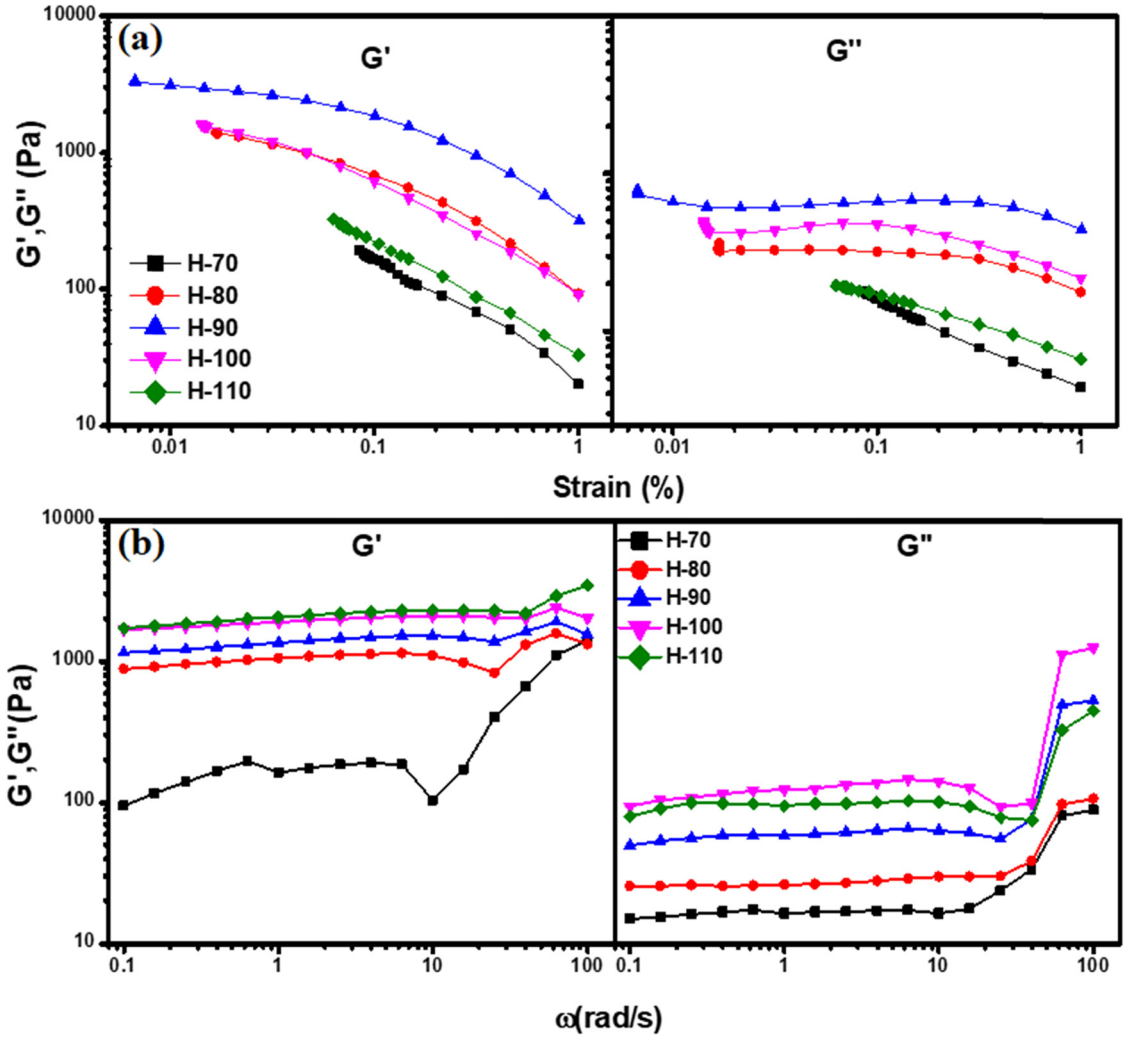

Figure 5: (a) Strain sweep test: G' and G'' modulus as a function of strain and (b) frequency sweep test: G′ and G″ modulus as a function of frequency.

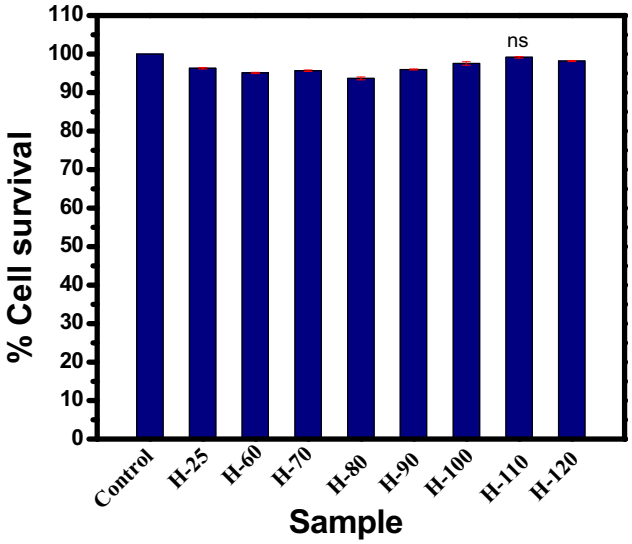

Figure 6: Cell viability study of hydrogel samples for 24 h. Vertical bars representing mean ± SEM. Significance was tested using one-way ANOVA followed by Tukey *post-hoc* test.

increase as we increase the temperature from 70 to 110°C (Figure 5(b)). The higher values of G′ over G″ indicate that the elastic component is predominant on the viscous one in a swiped frequency range.

3.4 Biological studies

3.4.1 Cell toxicity and cellular uptake analysis

BSA has been extensively used in biomedical applications due to its higher bioavailability, biocompatibility, and biodegradability properties [51]. Herein, our objective was to study the cytotoxicity aspect of synthesized BSA hydrogel using BSA at various temperatures. *In vitro*, the biocompatibility of all hydrogel samples, *i.e.*, H-25, H-60, H-70, H-80, H-90, H-100, H-110, H-120, and H-200. is studied and shown in Figure 6. The MTT assay results demonstrated that all samples showed the % cell survival between 93.6 and 99.16%, which suggests its excellent

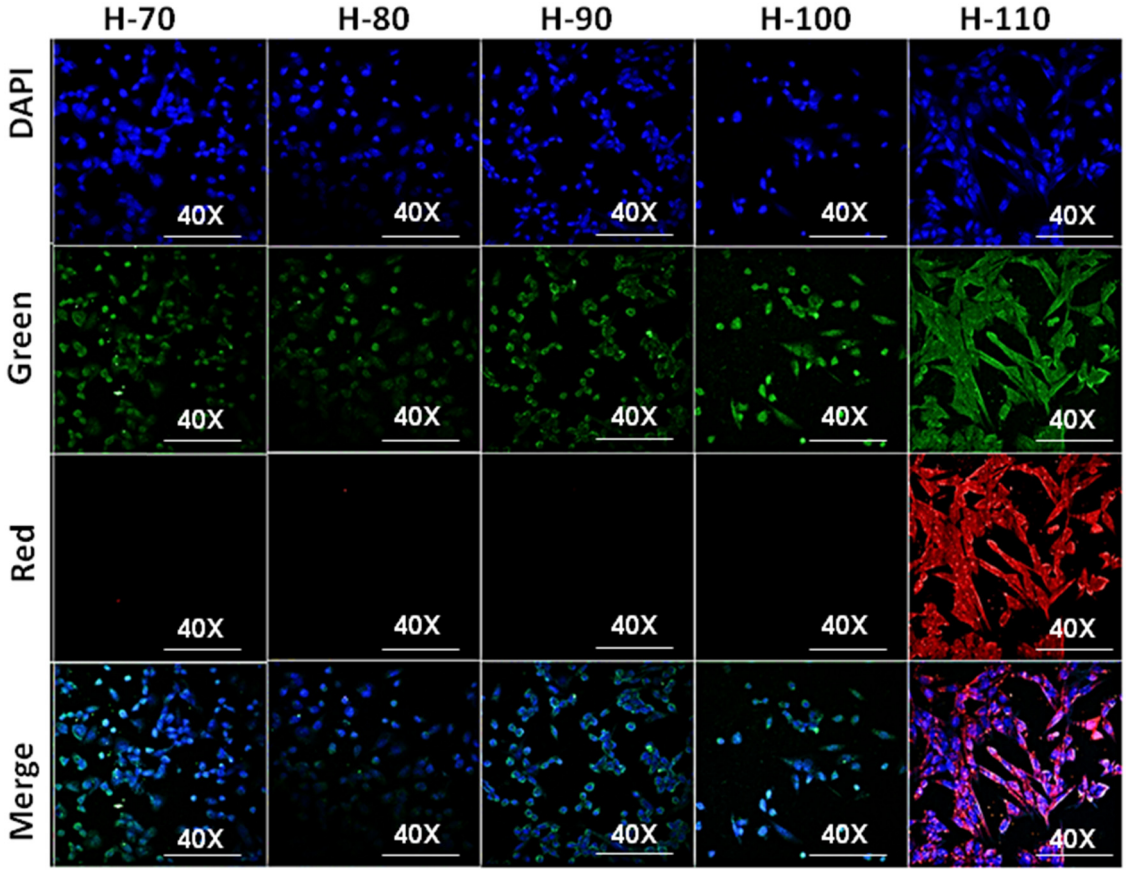

Figure 7: Confocal imaging of cellular uptake of H-60, H-70, H-80, H-90, H-100, and H-110.

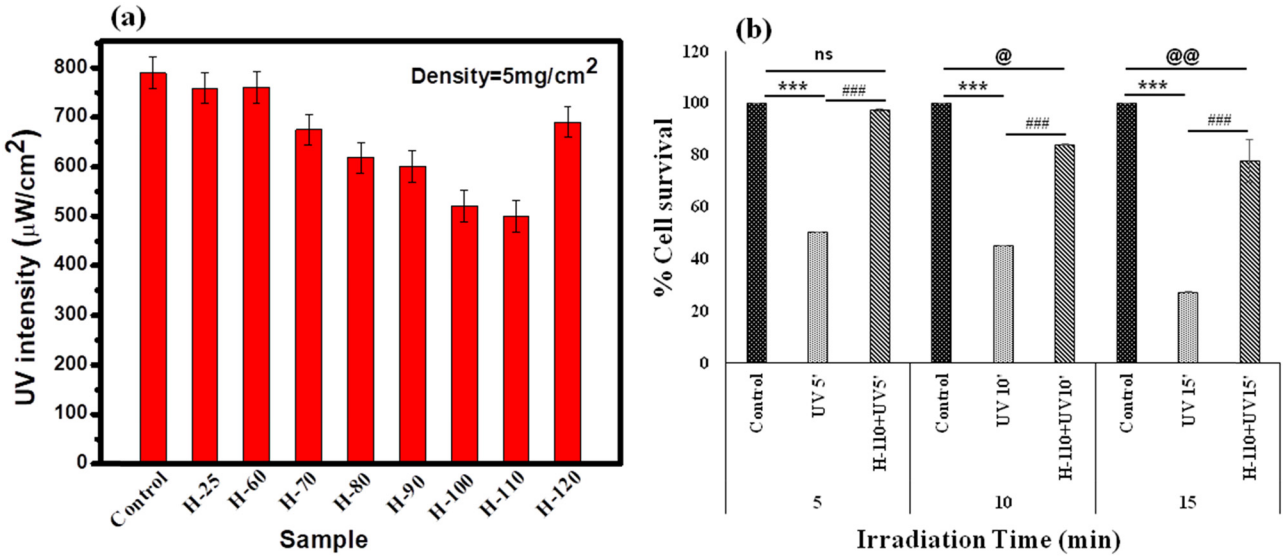

Figure 8: (a) UVB attenuation using different phases of BSA hydrogels, (b) protective role of H-110 from UVB-induced cytological damage primary skin cell culture by % cell viability assay, time-dependent experimental settings (5–15 min). Vertical bars representing mean ± SEM. Significance was tested using one-way ANOVA followed by Tukey Post-hoc test. The symbol * shows the significance level between control and only UVB, # shows the significance level between only UVB and H-110 + UVB, and @ shows the significance level between only control and H-110 + UVB. Data were considered statistically significant as ***/###/@@@ for $P < 0.0001$, **/##/@@ for $P < 0.01$, and */#/@ for $P < 0.05$.

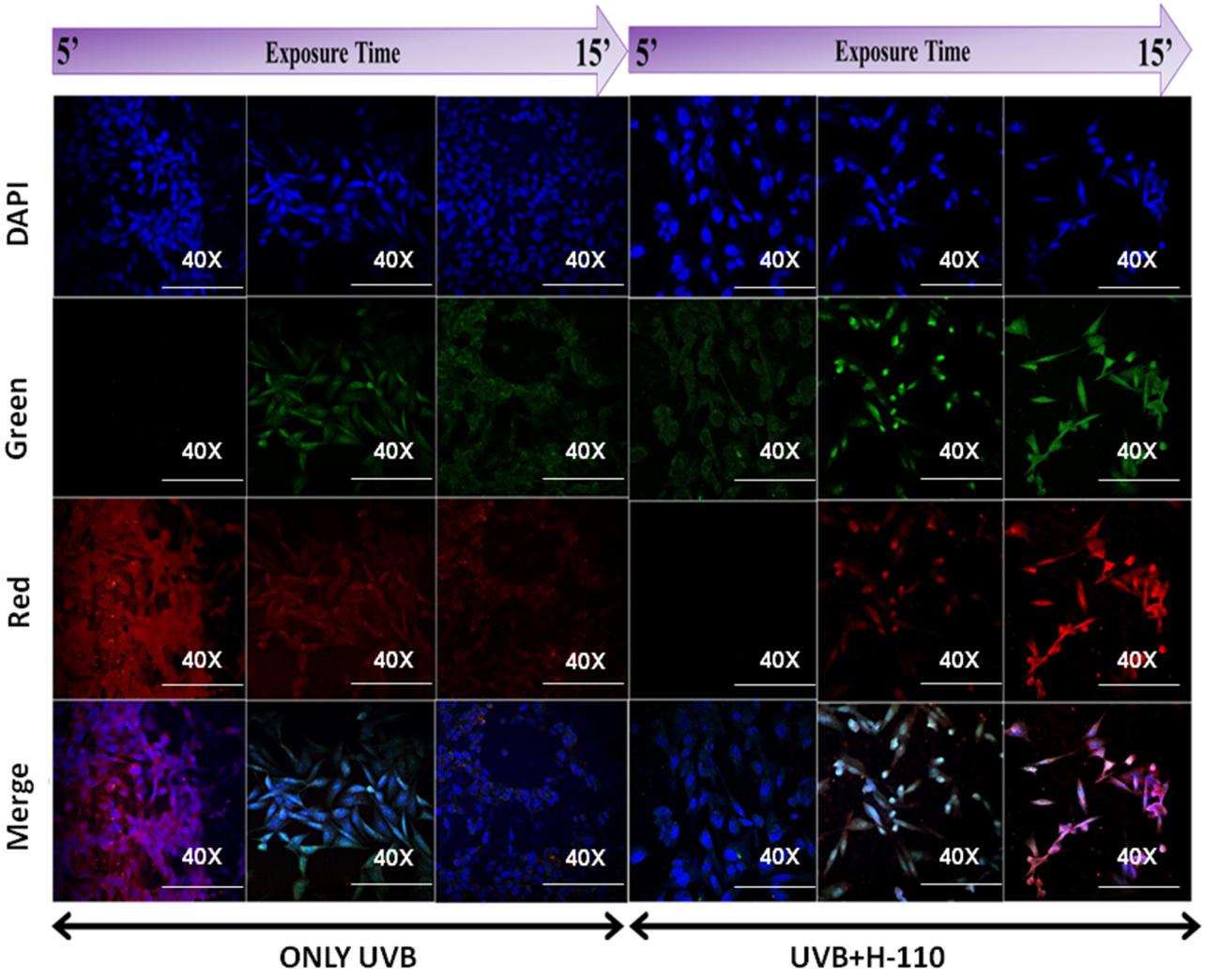

Figure 9: Protective role of H-110 from UVB-induced cytological damage primary skin cell culture by confocal bioimaging, time-dependent experimental settings (5–15 min).

biocompatibility. Among all of them, H-110 showed the highest % cell survival of 99.16%.

Cellular uptake studies further confirm its good bioimaging green autofluorescence capacity in all hydrogel samples. Interestingly, H-110 has shown maximum cellular penetration (Figure 7) with a higher cytoplasmic and nuclear distribution. Hence, we have applied H-110 for further experimental studies.

3.4.2 Studying the protective role of H-110 on UVB induced cytological damaged primary skin cells

UVB attenuation activity of all the samples is tested and shown in Figure 8(a). All the gel phases have shown a significant reduction in UVB intensity. However, maximum attenuation is shown by H-110 with a density of 5 mg/cm^2. The maximum UVB irradiance emitted by the UVB rod was 790 μW/cm^2 at 11 cm away from the rod where all the UV attenuation studies were performed. The maximum attenuation is observed by H-110 hydrogel with a 36.7% decrease. Our MTT data have demonstrated aggressive normal skin cell death except UVB treated cells after all three-time points, *i.e.*, 5, 10, and 15 min ($P < 0.000$, one-way ANOVA, followed by Tukey *post-hoc* test, Figure 8(b)). Minimum % cell survival was observed after 15 min UVB treatment (29.39 %) in comparison to control skin cells ($P < 0.000$, one-way ANOVA, followed by Tukey *post-hoc* test). No significant cell death was observed after 5 min UVB exposure in H-110 applied skin cells in comparison to control skin cells ($P = 0.997$, one-way ANOVA, followed by Tukey Posthoc test). After 20 and 15 min of UVB exposure, the H-110 applied cells showed 84.06 and 77.76% cell survival. Interestingly, the H-110 layer on skin cells significantly increased skin cell survival at 47.33, 39.09, and 50.36% after respective 5, 10, and 15 min UVB exposure ($P < 0.000$, one-way ANOVA, followed by Tukey Posthoc test) [52].

It was observed that the confocal imaging data (Figure 9) are also in the accordance with the results of the MTT assay with the protective role of H-110 after UVB treatment. In our study, with an increase of UVB exposure time to cells from 5 to 15 min, the intensity of emitted red fluorescence decreases. This might be due to the disruption of cellular components with increased time of UVB exposure as the morphology of cells was also changed toward dead cells at 15 min UVB

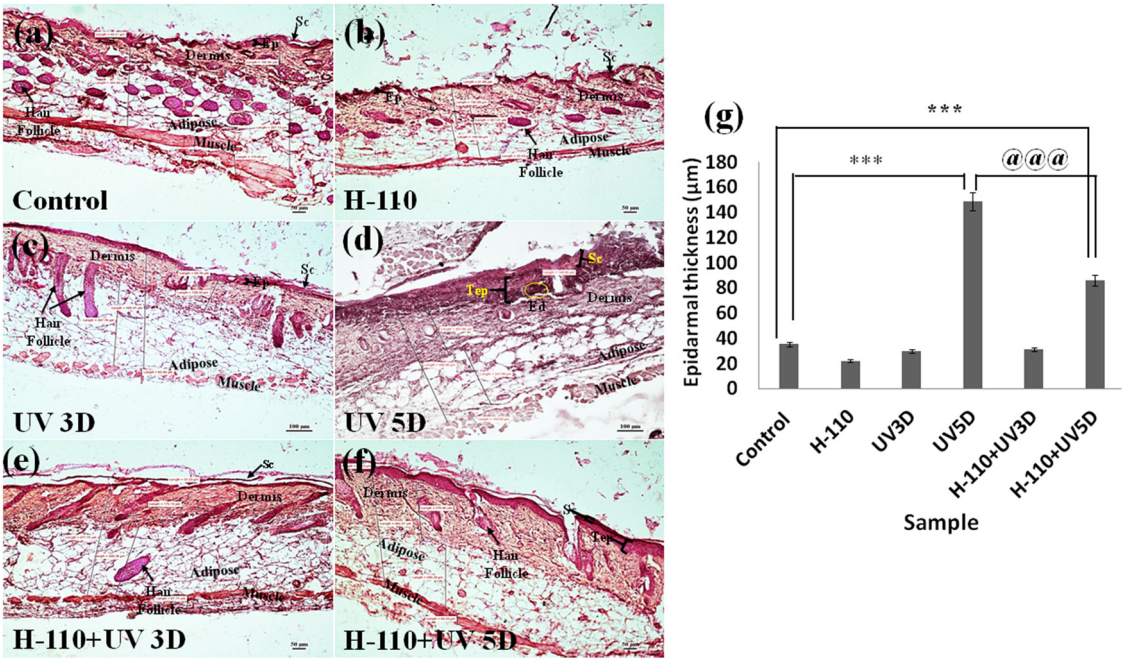

Figure 10: Transverse section showing histoarchitecture of skin tissue of *M. musculus*: (a) control, (b) H-110 treated, (c) UVB treated for 3 days, (d) UVB treated for 5 days, (e) H-110 + UV treated for 3 days, and (f) H-110 + UV treated for 5 days; Ep represents epidermis, Sc represents stratum corneum, Tep represents thickening epidermis, and Ed represents edema. (g) The vertical bar represents the epidermal thickness of different treatment groups (mean ± SEM). Significance was tested using one-way ANOVA followed by Tukey *post-hoc* test. The symbol * shows the significance level between control and only UVB 5 days, # shows the significance level between control and H-110 + UVB 5 days, and @ shows the significance level between only UVB 5 days and H-110 + UVB 5 days. Data were considered statistically significant as ***/###/@@@ for $P < 0.0001$.

exposed group. Previous studies have reported that the cell partially absorbs the smaller UV wavelength and emit a longer wavelength [52,53]. However, in the case of the H-110 applied group of cells, there was no significant morphological changes were observed after UVB exposure. Hence, this clearly shows that H-110 has the potential to protect the skin cells from UVB exposure.

3.4.3 *In vivo* protective role of H-110 on UVB-induced skin damage in mice

Our histological results with 3 days of UVB exposure (Figure 10(c)) showed no significant change, whereas 5 days of UVB exposure (Figure 10(d)) produced pathomorphological changes in the skin of mice, *i.e.*, significant thickening of stratum corneum (SC) and epidermis (Tep, $P < 0.000$), and perivascular edema (Ed) in the dermis was prominent. At H-110, the monolayer applied group showed no significant morphometric changes after 3 days of UVB exposure (Figure 10(e)). Interestingly, 5 days of UVB exposure at H-110 monolayer (Figure 10(f)) applied group showed significant epidermal thickening as compared with the control tissues ($P < 0.007$); however, when the epidermal thickness of H110 + UV5D skin tissues was compared with the epidermal thickness of the UV5D skin tissue, the epiderma was significantly thinner in the H-110 + UV5D skin tissue ($P < 0.000$, Figure 10(g)). Hence, our mice model study also supports our finding that the topical administration of H-110 is potentially effective in protecting the skin from UVB-induced skin damage.

4 Conclusion

Using a simple and efficient hydrothermal method, a wide range of phases varying from sol–gel–sol of BSA hydrogel were synthesized. This is the first-of-this-kind of study wherein we observed that even without using cross-linkers, we can synthesize different phases of protein by varying the hydrothermal temperature. Extensive physico-chemical and optical characterization data of synthesized hydrogels has shown its potential application as a UVB blocker for skin protection. To ensure, *in vitro* cytotoxicity and UV protection ability of hydrogels were tested using primary skin cells. Among all, the H-110 sample has shown extraordinary applicability. Thus, *in vivo* protective role of H-110 on UVB-induced skin damage in the mice model was studied, and the results have confirmed that the topical administration of H-110 is potentially effective in protecting the skin from UVB-induced skin damages. The present study ensures that using BSA protein as a precursor, it is possible to prepare hydrogels with various functionalities, no cytotoxicity and it holds a prominent role in the biomedical field for the protection of skin and in the cure of skin cancer.

Funding information: The authors would like to thank the Department of Science and Technology (SERB), India-CRG/2019/000903 (Core research Grant) & SB/S2/RJN-140/2014 (Ramanujan Fellowship Award) for the financial support of this study.

Author contributions: Kanchan Yadav: Conception or design of the work, data collection, data analysis, and interpretation, drafting the article; Megha Das: data collection, data analysis, and interpretation, drafting the manuscript; Nitesh Kumar Mishra: data collection; Anuj Chhabra: data collection, data analysis, and interpretation; Archana Mishra: drafting the manuscript, data analysis and interpretation; Sunita Srivastava: data analysis and interpretation; Poonam Sharma: resource, editing of the manuscript; Sanjeev Kumar Yadav: data analysis and interpretation; Avanish Singh Parmar: conception or design of the work, drafting of the manuscript, funding, and resources. All authors have accepted responsibility for the entire content of this manuscript and approved its submission.

Conflict of interest: The authors state no conflict of interest.

Ethical approval: All maintenance procedures along with experimentations were performed following the revised Animals Act Government of India, 2007 approved rules [Committee for the Purpose of Control and Supervision of Experiments on Animals (CPCSEA), Registration No.-1802/GO/Re/S/15/CPCSEA].

References

[1] D'Orazio J, Jarrett S, Amaro-Ortiz A, Scott T. UV radiation and the skin. Int J Mol Sci. 2013;14(6):12222–48. doi: 10.3390/ijms140612222.

[2] Sanford JA, Gallo RL. Functions of the skin microbiota in health and disease. Semin Immunol. 2013;25(5):370. doi: 10.1016/J.SMIM.2013.09.005.

[3] Med CC. Ultraviolet radiation exposure and its impact on skin cancer risk. 2015;40(4):1291–6. doi: 10.1097/CCM.0b013e31823da96d.Hydrogen.

[4] Teresa M, Petersen S, Prakash G. UV light effects on proteins: from photochemistry to nanomedicine. Mol Photochem – Var Asp. 2012;37947:1–36. doi: 10.5772/37947.
[5] Harrison SC, Bergfeld WF. Ultraviolet light and skin cancer in athletes. Sports Health. 2009;1(4):335–40. doi: 10.1177/1941738109338923.
[6] Craig S, Earnshaw CH, Virós A. Ultraviolet light and melanoma. J Pathol. 2018;244(5):578–85. doi: 10.1002/path.5039.
[7] Fontanillas P, Alipanahi B, Furlotte NA, Johnson M, Wilson CH, Pitts SJ, et al. Disease risk scores for skin cancers. Nat Commun. 2021;12(1):1–13. doi: 10.1038/s41467-020-20246-5.
[8] Siegel RL, Miller KD, Fuchs HE, Jemal A. Cancer statistics, 2021. CA Cancer J Clin. 2021;71(1):7–33. doi: 10.3322/CAAC.21654.
[9] Nehal KS, Bichakjian CK. Update on keratinocyte carcinomas. N Engl J Med. 2018;379(4):363–74. doi: 10.1056/NEJMRA1708701/SUPPL_FILE/NEJMRA1708701_DISCLOSURES.PDF.
[10] Diepgen TL, Mahler V. The epidemiology of skin cancer. Br J Dermatol. 2002;146(s61):1–6. doi: 10.1046/J.1365-2133.146.S61.2.X.
[11] Xu L, Wu D, Zhou B, Xu Y, Wang W, Yu D, et al. Microencapsulated sunblock nanoparticles based on zeolitic imidazole frameworks for safe and effective UV protection. RSC Adv. 2018;8(22):12315–21. doi: 10.1039/c8ra00632f.
[12] Pristovnik M, Maver U, Orthaber K, Skok K, Perić B. Skin cancer and its treatment: novel treatment approaches with emphasis on nanotechnology. J Nanomater. 2017;2017:1–20. doi: 10.1155/2017/2606271.
[13] Jose J, Netto G. Role of solid lipid nanoparticles as photoprotective agents in cosmetics. J Cosmet Dermatol. 2019;18(1):315–21. doi: 10.1111/jocd.12504.
[14] Lu PJ, Fang SW, Cheng WL, Huang SC, Huang MC, Cheng HF. Characterization of titanium dioxide and zinc oxide nanoparticles in sunscreen powder by comparing different measurement methods. J Food Drug Anal. 2018;26(3):1192–200. doi: 10.1016/J.JFDA.2018.01.010.
[15] Singh P, Nanda A. Enhanced sun protection of nano-sized metal oxide particles over conventional metal oxide particles: an in vitro comparative study. Int J Cosmet Sci. 2014;36(3):273–83. doi: 10.1111/ICS.12124.
[16] Vitiello G, Zanfardino A, Tammaro O, Di Napoli M, Caso MF, Pezzella A, et al. Bioinspired hybrid eumelanin-TiO_2 antimicrobial nanostructures: the key role of organo-inorganic frameworks in tuning eumelanin's biocide action mechanism through membrane interaction. RSC Adv. 2018;8(50):28275–83. doi: 10.1039/c8ra04315a.
[17] Wu MS, Sun DS, Lin YC, Cheng CL, Hung SC, Chen PK, et al. Nanodiamonds protect skin from ultraviolet B-induced damage in mice. J Nanobiotechnol. 2015;13(1):1–12. doi: 10.1186/s12951-015-0094-4.
[18] Vishnubhakthula S, Elupula R, Durán-Lara EF. Recent advances in hydrogel-based drug delivery for melanoma cancer therapy: a mini review. J Drug Deliv. 2017;2017:1–9. doi: 10.1155/2017/7275985.
[19] Rigon RB, Oyafuso MH, Fujimura AT, Gonçalez ML, Prado AH, Gremião MP, et al. Nanotechnology-based drug delivery systems for melanoma antitumoral therapy: a review. Biomed Res Int. 2015;2015:16–20. doi: 10.1155/2015/841817.
[20] Tang JQ, Hou XY, Yang CS, Li YX, Xin Y, Guo WW, et al. Recent developments in nanomedicine for melanoma treatment. Int J Cancer. 2017;141(4):646–53. doi: 10.1002/ijc.30708.
[21] Vyas A, Das SK, Singh D, Sonker A, Gidwani B, Jain V, et al. Recent nanoparticuulate approches of drug delivery for skin cancer. Trends Appl Sci Res. 2012;7:620–35.
[22] Chang Z, Zhang S, Li F, Wang Z, Li J, Xia C, et al. Self-healable and biodegradable soy protein-based protective functional film with low cytotoxicity and high mechanical strength. Chem Eng J. 2021;404:126505. doi: 10.1016/J.CEJ.2020.126505.
[23] Kumar M, Sanford KJ, Cuevas WP, Du M, Collier KD, Chow N. Designer protein-based performance materials. Biomacromolecules. 2006;7(9):2543–51. doi: 10.1021/BM060464A.
[24] Debele TA, Su WP. Polysaccharide and protein-based functional wound dressing materials and applications. 2020;71:87–108. doi: 10.1080/00914037.2020.1809403.
[25] Zhang D, Wang Y. Functional protein-based bioinspired nanomaterials: from coupled proteins, synthetic approaches, nanostructures to applications. Int J Mol Sci. 2019;20(12):3054. doi: 10.3390/IJMS20123054.
[26] Mahler A, Reches M, Rechter M, Cohen S, Gazit E. Rigid, Self-assembled hydrogel composed of a modified aromatic dipeptide. Adv Mater. 2006;18(11):1365–70. doi: 10.1002/ADMA.200501765.
[27] Nagarajan S, Radhakrishnan S, Kalkura S, Balme S, Miele P, Bechelany M. Overview of protein-based biopolymers for biomedical application. Macromol Chem Phys. 2019;220(14):1900126. doi: 10.1002/MACP.201900126.
[28] Xing Y, Cheng E, Yang Y, Chen P, Zhang T, Sun Y, et al. Self-assembled dna hydrogels with designable thermal and enzymatic responsiveness. Adv Mater. 2011;23(9):1117–21. doi: 10.1002/adma.201003343.
[29] Arabi SH, Aghelnejad B, Schwieger C, Meister A, Kerth A, Hinderberger D. Biomaterials science rsc.li/biomaterials-science serum albumin hydrogels in broad pH and temperature ranges: characterization of their self-assembled structures and nanoscopic and macroscopic properties. Biomater Sci. 2018;6:478. doi: 10.1039/c7bm00820a.
[30] Su TJ, Lu JR, Thomas RK, Cui ZF, Penfold J. The conformational structure of bovine serum albumin layers adsorbed at the silica–water interface. J Phys Chem B. 1998;102(41):8100–8. doi: 10.1021/JP981239T.
[31] Jayabharathi J, Thanikachalam V, Venkatesh Perumal M. Mechanistic investigation on binding interaction of bioactive imidazole with protein bovine serum albumin—a biophysical study. Spectrochim Acta Part A Mol Biomol Spectrosc. 2011;79(3):502–7. doi: 10.1016/J.SAA.2011.03.020.
[32] Wu X, Lv L, Han X, Li C. Bovine serum albumin fibrous biofilm template synthesis of metallic nanomeshes for surface-enhanced Raman scattering and electrocatalytic detection. Mater Des. 2020;192:108777. doi: 10.1016/J.MATDES.2020.108777.
[33] Yuan H, Zheng X, Liu W, Zhang H, Shao J, Yao J, et al. A novel bovine serum albumin and sodium alginate hydrogel scaffold doped with hydroxyapatite nanowires for cartilage defects repair. Colloids Surfaces B Biointerfaces. 2020;192:111041. doi: 10.1016/J.COLSURFB.2020.111041.
[34] Zewde B, Atoyebi O, Gugssa A, Gaskell KJ, Raghavan D. An investigation of the interaction between bovine serum albumin-conjugated silver nanoparticles and the hydrogel in hydrogel nanocomposites. ACS Omega. 2021;6(17):11614–27. doi: 10.1021/ACSOMEGA.1C00834/SUPPL_FILE/AO1C00834_SI_001.PDF.
[35] Upadhyay A, Narula A, Rao CP. Copper-based metallogel of bovine serum albumin and its derived hybrid biomaterials as

aerogel and sheet: comparative study of the adsorption and reduction of dyes and nitroaromatics. ACS Appl Bio Mater. 2020;3(12):8619–26. doi: 10.1021/ACSABM.0C01028/SUPPL_FILE/MT0C01028_SI_001.PDF.

[36] Phan VHG, Le TMD, Janarthanan G, Ngo PKT, Lee DS, Thambi T. Development of bioresorbable smart injectable hydrogels based on thermo-responsive copolymer integrated bovine serum albumin bioconjugates for accelerated healing of excisional wounds. J Ind Eng Chem. 2021;96:345–55. doi: 10.1016/J.JIEC.2021.01.041.

[37] Henrot P, Laurent P, Levionnois E, Leleu D, Pain C, Truchetet ME, et al. A method for isolating and culturing skin cells: application to endothelial cells, fibroblasts, keratinocytes, and melanocytes from punch biopsies in systemic sclerosis skin. Front Immunol. 2020;11:2408. doi: 10.3389/FIMMU.2020.566607.

[38] Yadav K, Das M, Hassan N, Mishra A, Lahiri J, Dubey A, et al. Synthesis and characterization of novel protein nanodots as drug delivery carriers with an enhanced biological efficacy of melatonin in breast cancer cells. RSC Adv. 2021;11(16):9076–85. doi: 10.1039/D0RA08959A.

[39] Shukla D, Das M, Kasade D, Pandey M, Dubey AK, Yadav SK, et al. Sandalwood-derived carbon quantum dots as bioimaging tools to investigate the toxicological effects of malachite green in model organisms. Chemosphere. 2020;248:125998. doi: 10.1016/j.chemosphere.2020.125998.

[40] Jiang B, Jain A, Lu Y, Hoag SW. Probing thermal stability of proteins with temperature scanning viscometer. Mol Pharm. 2019;16(8):3687–93. doi: 10.1021/ACS.MOLPHARMACEUT.9B00598.

[41] Michnik A, Michalik K, Drzazga Z. Stability of bovine serum albumin at different pH. J Therm Anal Calorim. 2005;80(2):399–406. doi: 10.1007/S10973-005-0667-9.

[42] Molodenskiy D, Shirshin E, Tikhonova T, Gruzinov A, Peters G, Spinozzi F. Thermally induced conformational changes and protein–protein interactions of bovine serum albumin in aqueous solution under different pH and ionic strengths as revealed by SAXS measurements. Phys Chem Chem Phys. 2017;19(26):17143–55. doi: 10.1039/C6CP08809K.

[43] Ma X, Sun X, Hargrove D, Chen J, Song D, Dong Q, et al. A biocompatible and biodegradable protein hydrogel with green and red autofluorescence: preparation, characterization and in vivo biodegradation tracking and modeling. Sci Rep. 2016;6(1):1–12. doi: 10.1038/srep19370.

[44] Arabi SH, Aghelnejad B, Schwieger C, Meister A, Kerth A, Hinderberger D. Serum albumin hydrogels in broad pH and temperature ranges: characterization of their self-assembled structures and nanoscopic and macroscopic properties. Biomater Sci. 2018;6(3):478–92. doi: 10.1039/C7BM00820A.

[45] Shibayama M, Tanaka T, Han CC. Small angle neutron scattering study on poly(N-isopropyl acrylamide) gels near their volume-phase transition temperature. J Chem Phys. 1998;97(9):6829. doi: 10.1063/1.463636.

[46] Hule RA, Nagarkar RP, Altunbas A, Ramay HR, Branco MC, Schneider JP, et al. Correlations between structure, material properties and bioproperties in self-assembled β-hairpin peptide hydrogels. Faraday Discuss. 2008;139:251. doi: 10.1039/B717616C.

[47] Surita S, Lackey MA, Griffin DM, Kishore S, Tew GN, Bhatia SR. SANS study of highly resilient poly(ethylene glycol) hydrogels. Soft Matter. 2014;10(12):1905–16. doi: 10.1039/C3SM52395K.

[48] Amdursky N, Mazo MM, Thomas MR, Humphrey EJ, Puetzer JL, St-Pierre JP, et al. Elastic serum-albumin based hydrogels: mechanism of formation and application in cardiac tissue engineering. J Mater Chem B. 2018;6(35):5604–12. doi: 10.1039/C8TB01014E.

[49] Bodenberger N, Kubiczek D, Abrosimova I, Scharm A, Kipper F, Walther P, et al. Evaluation of methods for pore generation and their influence on physio-chemical properties of a protein based hydrogel. Biotechnol Rep. 2016;12:6–12. doi: 10.1016/J.BTRE.2016.09.001.

[50] De Maria S, Ferrari G, Maresca P. Rheological characterization bovine serum albumin gels induced by high hydrostatic pressure. Food Nutr Sci. 2015;6(9):770–9. doi: 10.4236/FNS.2015.69080.

[51] Chen J, Ma X, Dong Q, Song D, Hargrove D, Vora SR, et al. Self-healing of thermally-induced, biocompatible and biodegradable protein hydrogel. RSC Adv. 2016;6(61):56183–92. doi: 10.1039/C6RA11239K.

[52] Allen M. Post hoc tests: tukey honestly significant difference test. SAGE Encycl Commun Res Methods. 2017;4:1–4. doi: 10.4135/9781483381411.N452.

[53] Notara M, Behboudifard S, Kluth MA, Maßlo C, Ganss C, Frank MH, et al. UV light-blocking contact lenses protect against short-term UVB-induced limbal stem cell niche damage and inflammation. Sci Rep. 2018;8(1):1–12. doi: 10.1038/S41598-018-30021-8.